metals

MDPI

Article

The Impact of Welding Parameters on the Welding Strength of High Borosilicate Glass and Aluminum Alloy

Changjun Chen [1,2], Jian Tang [1], Min Zhang [1,*] and Wei Zhang [3]

[1] Laser Processing Research Center, School of Mechanical and Electric Engineering, Soochow University, Suzhou 215131, China; chenchangjun@suda.edu.cn (C.C.); tangjian19980117@outlook.com (J.T.)
[2] State Key Laboratory of Advanced Welding and Joining, Harbin Institute of Technology, Harbin 150001, China
[3] Shi-Changxu Innovation Center for Advanced Materials, Institute of Metal Research, Chinese Academy of Sciences, Shenyang 110016, China; weizhang@imr.ac.cn
* Correspondence: zhangmin7822@suda.edu.cn; Tel.: +86-189-1551-7664

Abstract: This study adopts a new surface pretreatment method, Laser Surface Remelting (LSR). This experiment aims to establish a set of laser welding process parameters suitable for aluminum alloy and glass under this specific pretreatment. This experiment explores the impact of laser welding parameters on the welding strength between high borosilicate glass and aluminum alloy. The study specifically investigates the effects of four process parameters: defocus amount, laser power, frequency, and pulse width on the welding outcome. The results indicate that the welding quality between the aluminum alloy and glass reaches its optimum when the defocus amount is zero (i.e., when the laser converges at the interface between the glass and the metal) and the laser welding parameters are set to a power of 250 W, a welding speed of 1 mm/s, a welding frequency of 10 Hz, and a pulse width of 2.5 ms. The experiment also analyzes the fracture morphology under different parameters, summarizing the locations and causes of fractures, and establishing the relationship between the fracture location and the welding strength.

Keywords: glass; aluminum alloy; laser sealing process; microstructure; formation mechanism; laser parameters

Citation: Chen, C.; Tang, J.; Zhang, M.; Zhang, W. The Impact of Welding Parameters on the Welding Strength of High Borosilicate Glass and Aluminum Alloy. *Metals* **2024**, *14*, 1001. https://doi.org/10.3390/met14091001

Academic Editor: Dariusz Rozumek

Received: 26 July 2024
Revised: 24 August 2024
Accepted: 31 August 2024
Published: 2 September 2024

1. Introduction

Aluminum alloys and high borosilicate glass are important materials with broad application prospects in industrial and technological fields. For example, welding aluminum alloys with glass is used in manufacturing car body components, which can enhance the strength and lightweight properties of automotive structures.

High borosilicate glass has a very high silicon content and very low alkali content, with a boron oxide (B_2O_3) content exceeding 10%. This composition gives high borosilicate glass excellent optical and electrical properties, along with an extremely low coefficient of thermal expansion, high hardness, superior chemical resistance, and outstanding thermal shock resistance. The light transmittance of high borosilicate glass can reach over 90%, and its thermal expansion coefficient has a range of 32~40 $\times$ 10^{-7}/°C, which is only about one third that of ordinary glass. This makes it less prone to cracking when exposed to temperature changes, a characteristic that makes high borosilicate glass widely used in products such as solar water heater tubes, glass instruments, chemical pipelines, and heat-resistant glassware [1–4]. In this experiment, its excellent thermal shock resistance and low thermal expansion coefficient help ensure that the welded samples experience less stress and are less likely to develop cracks or other defects [5].

Aluminum alloy is a common metallic material known for its high strength, high toughness, high specific strength, and good machinability, making it widely used in large, lightweight structural components such as aerospace and automotive engine parts.

AlCu5Mn aluminum alloy, developed independently in China, is a high-strength, high-toughness cast aluminum alloy. Compared to other aluminum alloys, AlCu5Mn offers superior mechanical and processing properties, making it widely applied in large, load-bearing structural components. Although AlCu5Mn aluminum alloy has relatively low strength, it has good toughness, is easier to process, and generates less stress during welding. At the same time, it retains the corrosion resistance and lightweight characteristics typical of other aluminum alloys. These properties are the primary reasons for selecting AlCu5Mn aluminum alloy in this experiment [6–8].

Currently, the connection between glass and metal in most scenarios relies on adhesive bonding. However, this method often fails in high-temperature and heavy-load environments. Therefore, in recent years, many scholars have researched the welding of glass and metal. Laser welding, with its advantages of high speed, small weld seams, and precise welding, is a highly feasible welding solution [9–14]. Nevertheless, due to the significant differences in the chemical and physical properties of aluminum alloys and glass, welding them together has always been a challenging task. Appropriate surface pre-treatment processes greatly enhance the welding strength between aluminum alloys and glass.

Octav P. Ciuca et al. used a picosecond pulsed laser to perform precision welding of 1 mm thick quartz glass and 1 mm thick pure aluminum sheets and analyzed the welded joints. However, due to the high transient characteristics of multiple picosecond high-energy density laser pulses and the differences in the thermophysical properties of the two weld components, the process of rapidly applying multiple picosecond high-energy density laser pulses to form a weld is complex [15]. Lin et al. used a 1064 nm fiber laser to weld quartz glass and anodized aluminum alloy. Under optimal processing conditions, with a scanning speed of 100 m/s and laser power of 2 W, the welding interface displayed a dense, uniform, and void-free morphology with an adhesive strength of 8 kg. However, aluminum alloys require anodizing treatment, a complex process that demands strict control of process parameters to ensure a high-quality oxide film [16]. Qiu et al. found that with a 5 μm thick micro-arc oxidation film, the optimal welding parameters were a laser power of 100 W, a frequency of 10 Hz, and a pulse width of 2.5 ms, which resulted in the maximum shear strength of the glass–metal weld. However, the micro-arc oxidation process is more complex and not easy to produce [17]. Li et al. used an ink immersion staining method for aluminum alloy surface pre-treatment. However, due to the presence of a large quantity of organic substances in the blackening ink of the aluminum alloy, the ink participates in the reaction during welding. Organic substances tend to release hydrogen at high temperatures, which could be the cause of porosity in the weld [18].

Based on the research conducted by scholars, it can be observed that the current exploration of laser welding processes for aluminum alloys and glass mainly focuses on indirect welding methods, such as preparing micro-arc oxidation films on the surface and adding surface coatings. Although these methods can achieve a certain level of welding strength, their application is often limited due to the complexity of the process and the need to introduce additional elements. This study adopts a new surface pretreatment method, Laser Surface Remelting (LSR). LSR is a surface modification technique where the material's surface is rapidly melted by laser heating and subsequently cooled. This process can enhance the surface properties of the material, such as hardness, wear resistance, corrosion resistance, and fatigue resistance [19,20]. Since there is no documented research on the laser parameters under this pretreatment method, this experiment aims to establish a set of laser welding process parameters suitable for aluminum alloy and glass under this specific pretreatment.

According to the principles of laser welding, the process parameters that mainly affect the welding strength of high borosilicate glass and aluminum alloy include laser power, laser frequency, pulse width, and defocus amount [21–27]. The welding results were evaluated in the following three ways: first, studying the impact of different process parameters on the weld morphology of high borosilicate glass and aluminum alloy; second, recording and comparing the shear strength of high borosilicate glass and aluminum alloy

weldments under different process parameters; third, investigating the influence of different process parameters on the shear fracture morphology of the welding test samples. Based on the formation rules of weld and shear fracture morphology under different process parameters, the laser welding mechanism of high borosilicate glass and aluminum alloy, and the causes of shear fracture failure were analyzed and summarized.

2. Experimental Materials and Methods

2.1. Experimental Materials

In this experiment, the composition of AlCu5Mn is shown in Table 1 and the composition of high borosilicate glass is shown in Table 2.

Table 1. Composition of AlCu5Mn aluminum alloy (mass fraction %).

Al	Si	Cu	Mg	Mn
83.0–85.0	11.0–13.0	0.2–0.6	0.1	<0.1

Table 2. Composition of high borosilicate glass (mass fraction %).

SiO_2	Al_2O_3	CaO	MgO	Na_2O
70–73	0–3	6–12	0–4	12–16

Based on previous experiments, using a 250 W laser power for surface remelting before welding yielded better results. Therefore, this experiment is conducted under the premise of such pre-weld treatment.

2.2. Experimental Equipment

The primary equipment used in this study and their purposes are listed in Table 3.

Table 3. Experimental equipment and their uses.

Name	Model	Purpose
CNC Wire Cutting Machine	DK7732	Cutting metal samples
Ultrasonic Cleaning Machine	LTB-500	Cleaning samples
Vacuum Drying Oven	101-4	Drying experimental samples
Nd: YAG	MD-Focus300	Welding
Electronic Universal Testing Machine	RGM-4100	Shear strength testing
X-ray Photoelectron Spectroscopy (XPS)	EXCALAB 250 XI	Phase analysis
Scanning Electron Microscope (SEM)	EVO18	Morphological observation and spectroscopy
Grinding and Polishing Machine	MP-2A	Grinding and polishing samples
Confocal Colored Electron Microscope	OLS5000-SAF	Observing three-dimensional morphology
Spectrophotometer	7230G	Testing absorbance

The laser used in the experiment is an Nd: YAG, model MD-Focus300. The specifications are as follows:

- Wavelength: 1064 nm
- Pulse width: 0.1–20 ms
- Maximum frequency: 500 Hz
- Maximum power: 300 W

- Spot diameter: 0.2–20 mm
- Cooling system: Thermostatic closed-loop water cooling system
- Worktable travel range: 500 mm × 500 mm

The laser focusing lens used in the experiment has a focal length of 75 mm.

2.3. Experimental Method

In this experiment, aluminum alloy and glass were welded using an overlap joint configuration, as shown in Figure 1a. To evaluate the breaking strength of the current sealing samples, a method was developed based on ASTM F 734 (Standard Test Method for Shear Strength of Fusion Bonded Polycarbonate Aerospace Glazing Material) [28]. Since there is no directly applicable standard for glass-to-metal sealing, the specimen dimensions were tailored to the specific requirements of aerospace electronics, referencing the ASTM F 734 standard. The aluminum alloy was dimensioned at 18 mm × 14 mm × 3 mm, while the borosilicate glass was set at 18 mm × 14 mm × 1 mm. Shear tests were conducted to assess the bonding quality. A shear force test platform was designed, as illustrated in Figure 1b, and was mounted on the RGM-4100 electronic universal testing machine(Jinan Times Shijin Testing Machine Co., Ltd., Jinan, China). This shear testing machine, with a maximum force capacity of 4 kN, was used to evaluate the bonding strength of the glass-to-metal sealed samples. The tests were conducted at a constant speed of 1 mm/min until the samples failed. The breaking strength was determined by the force required to separate the sealed components. Due to variations in laser track width and depth, the effective bonding area differed for each set of parameters. To ensure accuracy, five samples produced under identical conditions were tested to determine the average breaking strength for each joint.

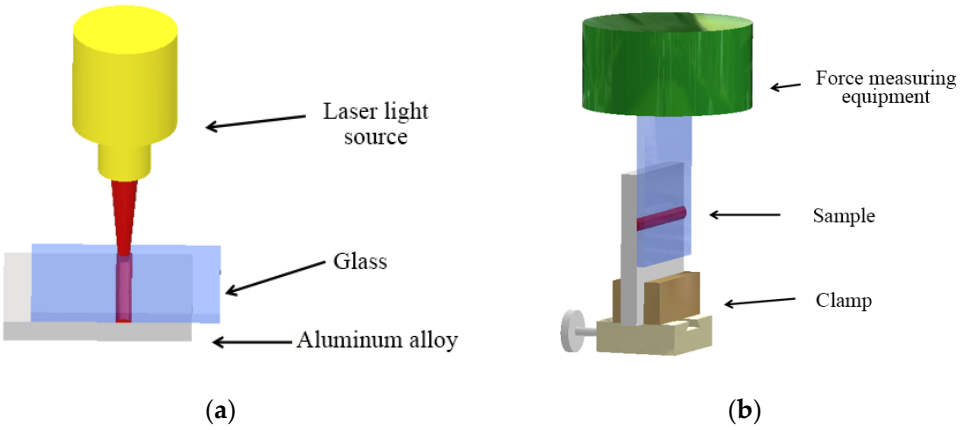

Figure 1. Schematic of welding and shear force test. (**a**) Welding diagram. (**b**) Shear test diagram.

The laser used in the welding experiment is an Nd: YAG. The energy density during operation is calculated using Equation (1).

$$\rho_N = \frac{E_p}{A} = \frac{4Pt_p}{\pi D^2} \tag{1}$$

where ρ_N is the energy density in joules per square millimeter (J/mm^2). E_p is the energy of the laser pulse in joules (J). A is the area of the laser spot. P is the maximum pulse power in watts (W). t_p is the pulse duration in seconds (s). D is the spot diameter in millimeters (mm) [29].

This experiment primarily investigates the effects of four parameters on welding strength:

- Laser Power
- Pulse Width
- Frequency
- Defocus Amount

The schematic diagram of the process flow is shown in Figure 2. The selection of parameters was fine-tuned based on the relevant literature [15–18]. With other parameters fixed, the influence of the variable parameters on welding strength was investigated. Accordingly, the welding experimental plan in Table 4 was designed.

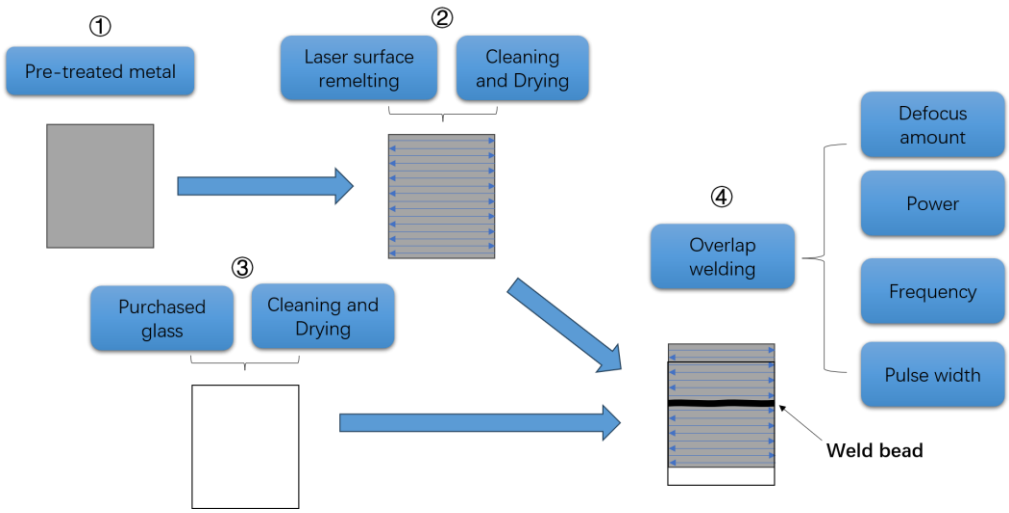

Figure 2. The schematic diagram of the process flow.

Table 4. Welding parameters for aluminum alloy and glass using laser welding.

Experiment Number	Power	Frequency	Pulse Width	Defocus Amount
1	250 W	10 Hz	2.5 ms	−1
2	250 W	10 Hz	2.5 ms	0
3	250 W	10 Hz	2.5 ms	1
4	250 W	10 Hz	2.5 ms	2
5	150 W	10 Hz	1.5 ms	0
6	200 W	10 Hz	1.5 ms	0
7	250 W	10 Hz	1.5 ms	0
8	300 W	10 Hz	1.5 ms	0
9	150 W	10 Hz	2.0 ms	0
10	200 W	10 Hz	2.0 ms	0
11	250 W	10 Hz	2.0 ms	0
12	300 W	10 Hz	2.0 ms	0
13	150 W	10 Hz	2.5 ms	0
14	200 W	10 Hz	2.5 ms	0
15	250 W	10 Hz	2.5 ms	0
16	300 W	10 Hz	2.5 ms	0
17	200 W	8 Hz	2.5 ms	0
18	200 W	10 Hz	2.5 ms	0
19	200 W	12 Hz	2.5 ms	0
20	200 W	14 Hz	2.5 ms	0
21	250 W	8 Hz	2.5 ms	0
22	250 W	10 Hz	2.5 ms	0
23	250 W	12 Hz	2.5 ms	0
24	250 W	14 Hz	2.5 ms	0
21	300 W	8 Hz	2.5 ms	0
22	300 W	10 Hz	2.5 ms	0
23	300 W	12 Hz	2.5 ms	0
24	300 W	14 Hz	2.5 ms	0
25	200 W	10 Hz	1.5 ms	0
26	200 W	10 Hz	2.0 ms	0

Table 4. *Cont.*

Experiment Number	Power	Frequency	Pulse Width	Defocus Amount
27	200 W	10 Hz	2.5 ms	0
28	200 W	10 Hz	3.0 ms	0
29	250 W	10 Hz	1.5 ms	0
30	250 W	10 Hz	2.0 ms	0
31	250 W	10 Hz	2.5 ms	0
32	250 W	10 Hz	3.0 ms	0
33	300 W	10 Hz	1.5 ms	0
34	300 W	10 Hz	2.0 ms	0
35	300 W	10 Hz	2.5 ms	0
36	300 W	10 Hz	3.0 ms	0

3. Experimental Results

3.1. Pre-Welding Surface Preparation

The metal surface is pre-treated as follows. First, the surface of the metal block is polished with 600-grit and 1000-grit sandpaper, then cleaned in an ultrasonic cleaning machine for 20 min, and finally dried. After treatment, the metal surface undergoes laser remelting. The laser power is 250 W, the focal distance is 0 mm, the scanning speed is 1 mm/s, the pulse width is 2.5 ms, and the pulse frequency is 10 Hz. The surface morphology before and after remelting and the cross-sectional morphology are shown in Figure 3.

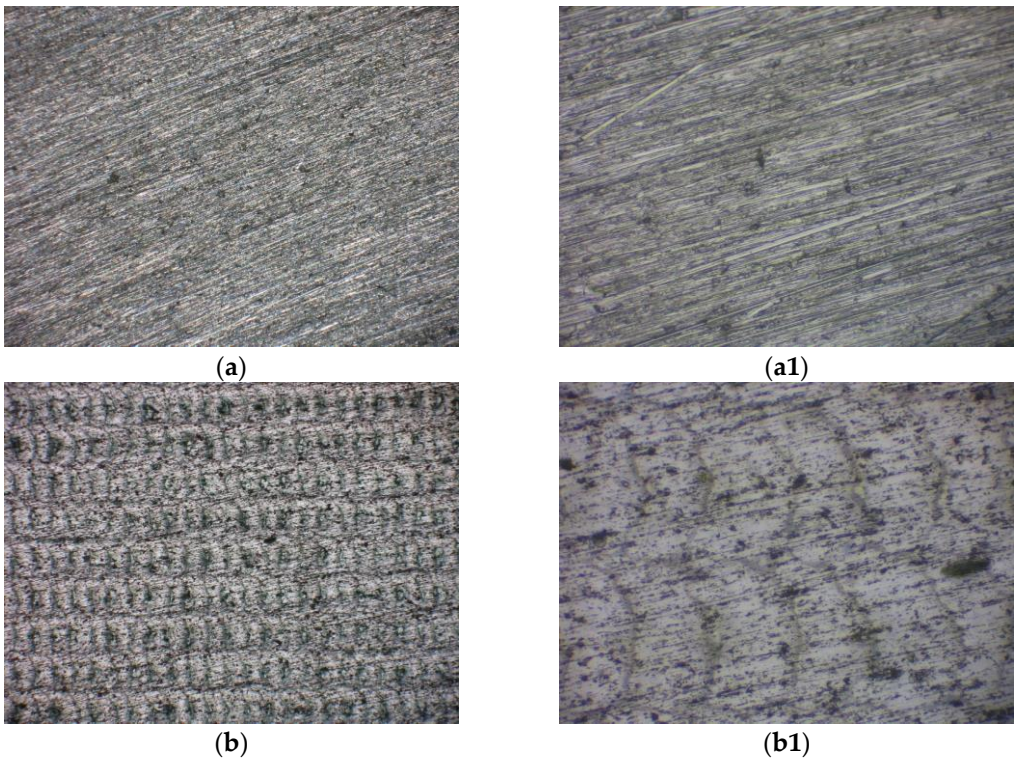

(**a**) (**a1**)

(**b**) (**b1**)

Figure 3. *Cont.*

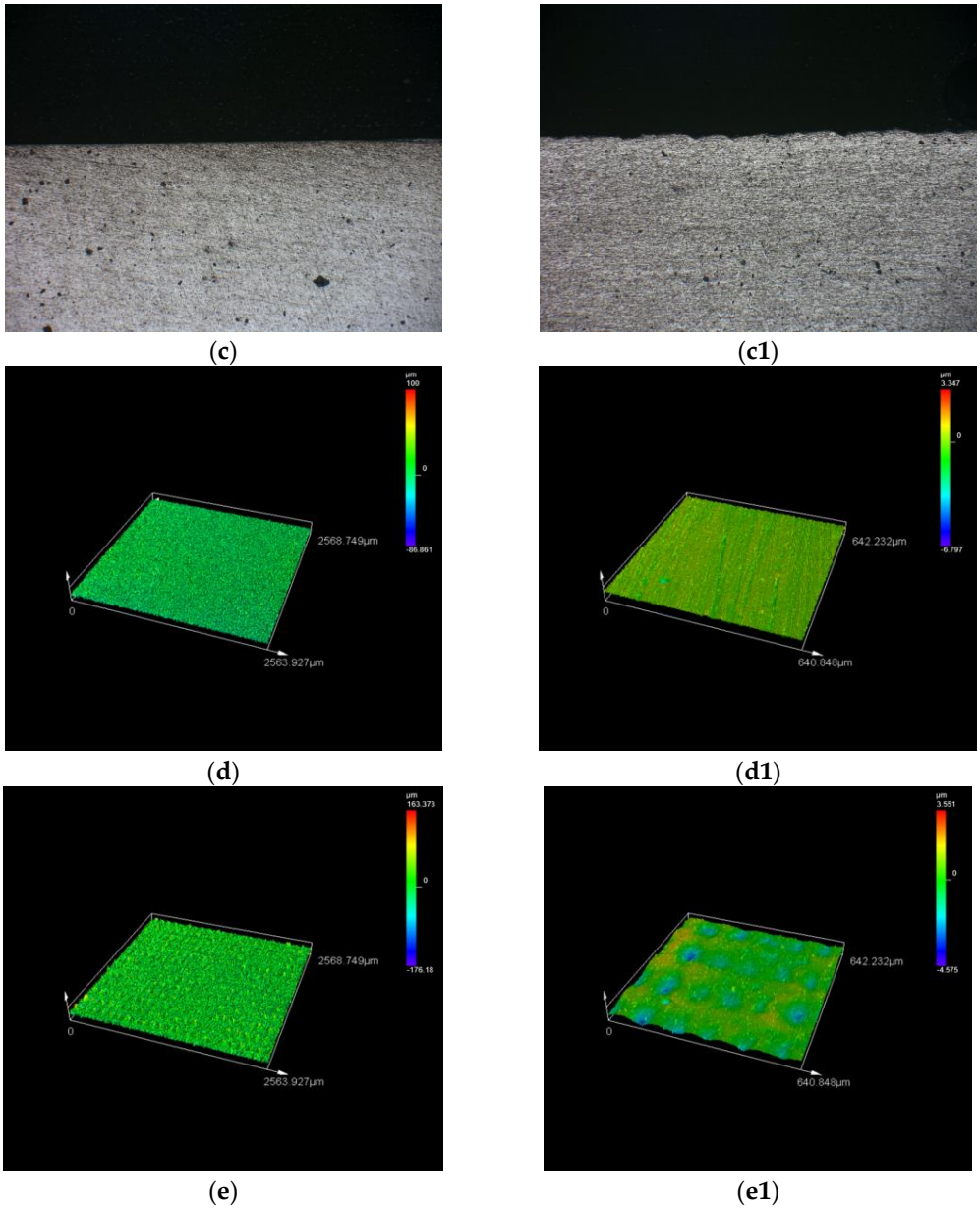

Figure 3. Surface and cross-sectional morphology. (**a**,**a1**) Before remelting. (**b**,**b1**) Surface after remelting. (**c**,**c1**) Cross-section after remelting. (**d**,**d1**) The three-dimensional morphology of the surface before remelting. (**e**,**e1**) The three-dimensional morphology of the surface after remelting. (**a**−**c**) Observed under optical microscope at 50× magnification. (**a1**−**c1**) Observed under optical microscope at 200× magnification.

3.2. Impact of Defocus Amount on Welding of High Borosilicate Glass and Aluminum Alloy

The laser spot of the Nd: YAG is formed by the convergence of multiple beams of light. Changing the defocus amount affects the position where the laser focuses during the welding process, which significantly impacts the amount of energy absorbed by the material being welded and, thereby, influences the welding seam. The effect of defocus amount on laser welding is primarily manifested in changes to the vertical position of the laser focus, as shown in Figure 4. Altering the vertical position of the laser focus changes the heat distribution during welding, which is a primary reason for the different welding outcomes observed. When the defocus amount is greater than 0, the focal point of the laser spot is above the metal surface, specifically, on the side of the glass. Conversely, when the defocus amount is negative, theoretically, the laser focus should penetrate into the interior

of the metal. However, since metals are generally not transparent, when the laser interacts with the sample, the spot area is larger, and the heating efficiency is lower compared to the scenario where the focal point is precisely on the metal surface.

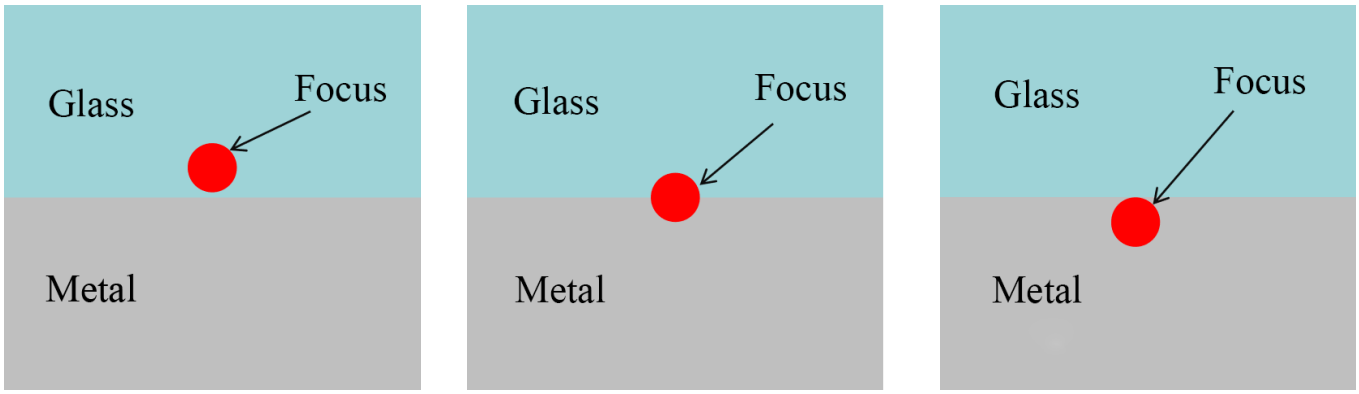

Figure 4. Laser-focus schematic diagram at different defocus amounts. (**a**) Defocus amount is less than 0. (**b**) Defocus amount is equal to 0. (**c**) Defocus amount is greater than 0.

The welding experiments were conducted with a fixed power of 150 W, frequency of 10 Hz, and pulse width of 2.5 ms, with defocus amounts set at −1 mm, 0 mm, +1 mm, and +2 mm. Figure 5 shows the cross-sectional images of the welds at different defocus amounts. From the figure, it can be observed that when the defocus amount is 0 mm, the depth of the weld pool is greater, and there are fewer defects such as cracks and voids. When the defocus amount is +2 mm, the size of the weld pool is relatively smaller. This is because the laser focus is further away from the interface between the glass and the metal, and the energy cannot be fully absorbed by the aluminum alloy surface, resulting in a smaller weld pool.

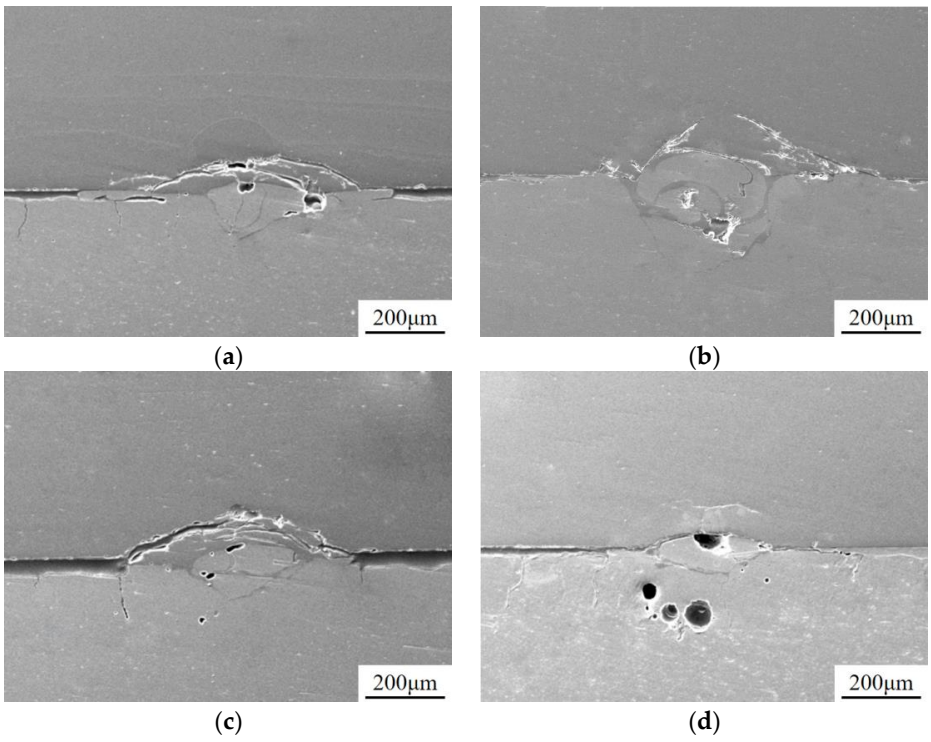

Figure 5. Welding cross-section images at different defocus amounts. (**a**) Defocus amount −1 mm. (**b**) Defocus amount 0 mm. (**c**) Defocus amount +1 mm. (**d**) Defocus amount +2 mm.

The samples welded at different defocus amounts were subjected to shear force testing using an RGM-4100 electronic universal testing machine. After testing, the fracture surfaces were observed under a SEM, as shown in Figure 6. From the figure, it can be observed that as the defocus amount increases, the width of the weld fracture surface initially increases and then decreases. When the defocus amount is 0 mm, the width of the weld fracture surface is the largest, and the splashed aluminum alloy is more uniform. Additionally, there are more metallic splashes left on the glass surface.

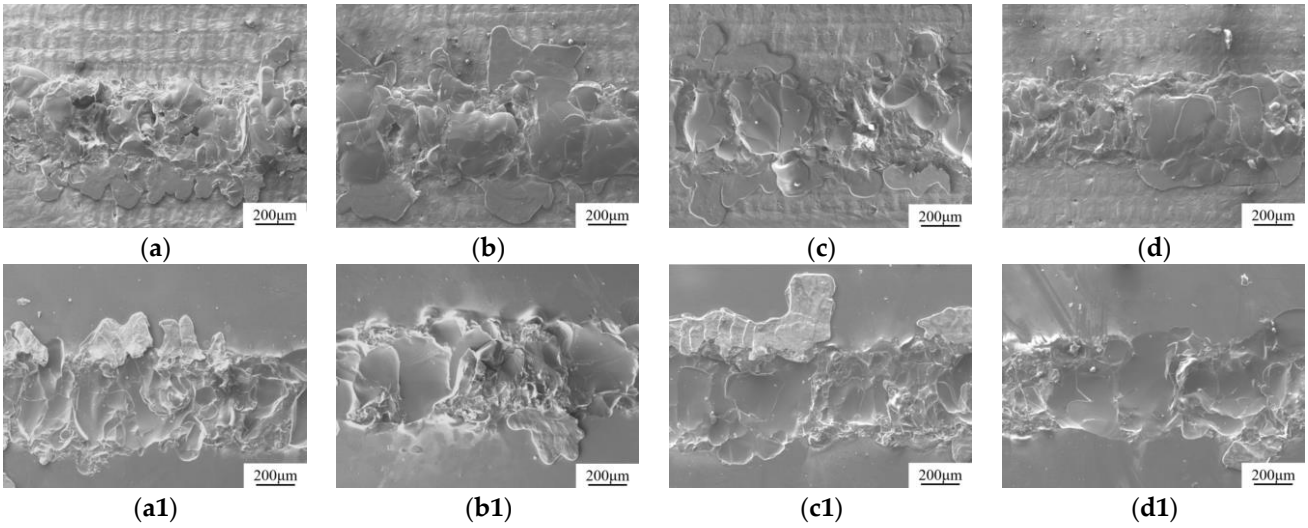

Figure 6. Welding cross-section images at different defocus amounts. (**a**,**a1**) Defocus amount −1 mm. (**b**,**b1**) Defocus amount 0 mm. (**c**,**c1**) Defocus amount +1 mm. (**d**,**d1**) Defocus amount +2 mm. (**a**–**d**) Metal side. (**a1**–**d1**) Glass side.

The results of shear force versus defocus amount are shown in Figure 7. From the figure, it can be observed that as the defocus amount increases, the shear force initially increases and then decreases. The reason for this phenomenon is analyzed as follows: when the defocus amount is negative, the laser cannot converge the beam effectively, resulting in lower heating efficiency. After welding to form a molten pool, the molten aluminum alloy overflows upward, raising the height of the processed surface. This disperses the beam further, reducing heating efficiency even more, as shown in Figure 8. As the defocus amount continues to increase to a certain extent, the focal point moves too far away from the material being welded, making it difficult to achieve the necessary heating for welding, thus reducing welding quality.

Considering both the weld seam and fracture morphology, as well as the comparison of welding strength, the welding effect is optimal when the defocus amount is 0 mm. In the subsequent exploration of laser-related process parameters, experiments were consistently conducted with a defocus amount of 0 mm.

3.3. Influence of Power on Welding Strength of Glass and Aluminum Alloy

In the initial exploratory experiments, it was found that changes in laser power have a significant impact on welding. This is mainly reflected in how changes in laser power affect the input energy, thereby influencing penetration depth and weld width. Keeping other welding parameters constant (frequency 10 Hz, pulse width 2.5 ms, defocus amount 0 mm, and welding speed 1 mm/s), only the power was varied sequentially: 150 W, 200 W, 250 W, and 300 W, as shown in Table 4 under serial numbers 5 to 16. The cross-sectional morphology of the weld at different powers is shown in Figure 9. From the figure, it can be observed that with increasing power, the penetration depth increases continuously, along with an increase in cracks. Moreover, defects such as pores in the weld seam also increase gradually, and cracks appear on the glass side at 300 W.

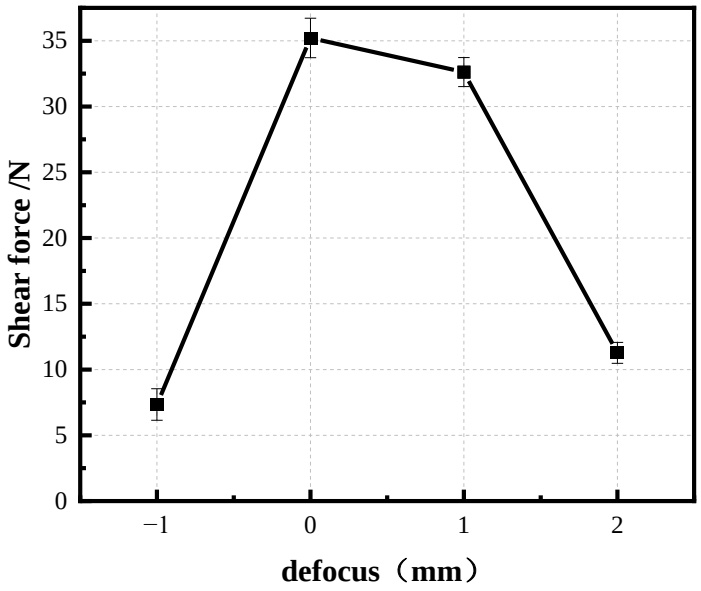

Figure 7. Shear force of test sample as a function of defocus amount.

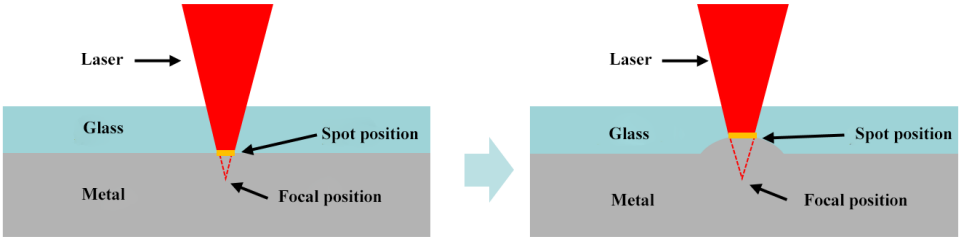

Figure 8. Variation of beam focusing effect during welding process with negative defocus.

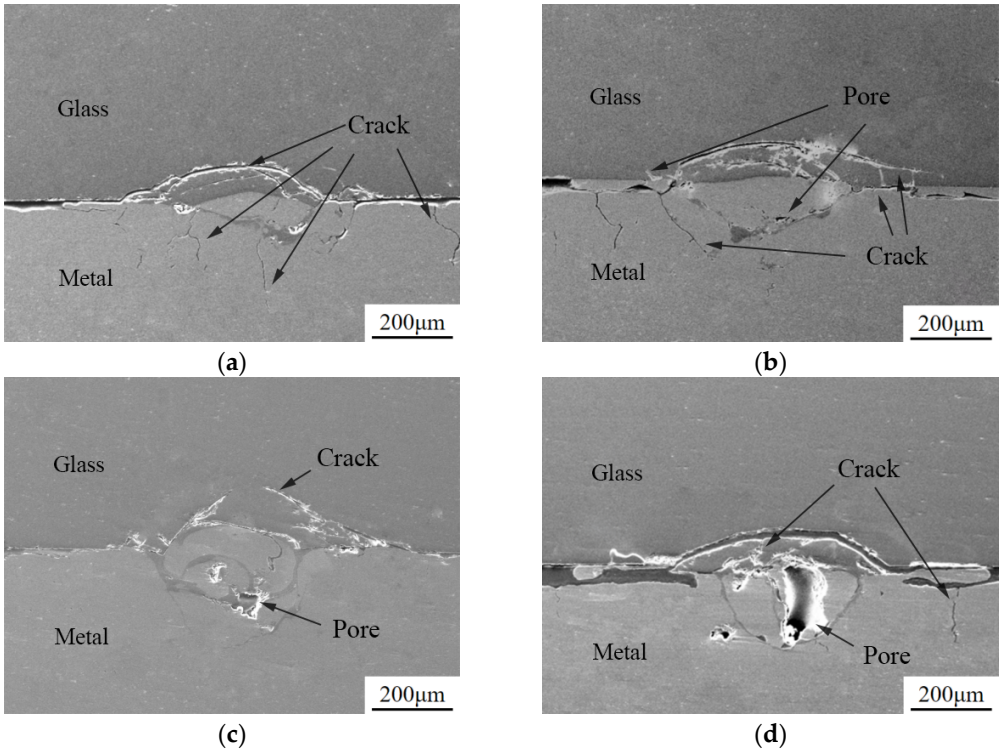

Figure 9. Weld seam morphology at different laser powers. (**a**) Laser power 150 W. (**b**) Laser power 200 W. (**c**) Laser power 250 W. (**d**) Laser power 300 W.

As shown in Figure 10, after the fracture and separation of high borosilicate glass and aluminum alloy, debris is produced that remains on the surfaces of both the glass and aluminum alloy. Therefore, after fracture and separation, the weld interface between the glass side and the aluminum alloy side is not completely aligned. From the figure, it can be observed that with increasing power, the fracture surface widens significantly, and there is a noticeable increase in splattering. Additionally, it can be seen that with increasing power, the amount of adhered material on the aluminum alloy side gradually increases, while on the glass side, it decreases.

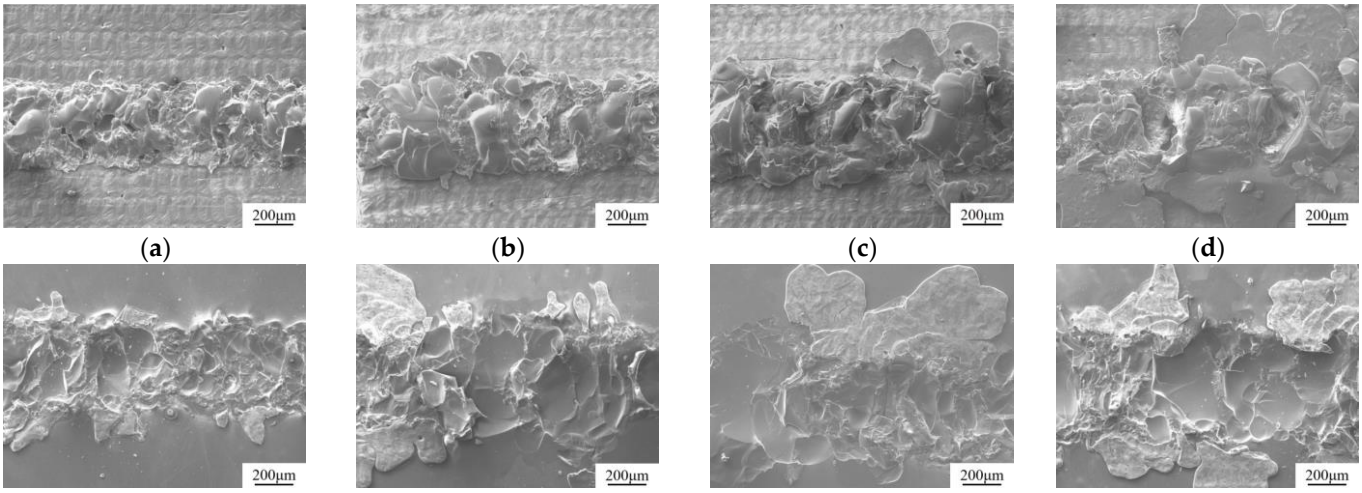

Figure 10. Welding cross-section images at different powers. (**a**,**a1**) Laser power 150 W. (**b**,**b1**) Laser power 200 W. (**c**,**c1**) Laser power 250 W. (**d**,**d1**) Laser power 300 W. (**a**–**d**) Metal side. (**a1**–**d1**) Glass side.

Due to the effect of pulse width on energy input, to ensure experimental accuracy, welding experiments were conducted under conditions of 2.0 ms and 1.5 ms pulse widths. Welded samples were tested for shear strength using a universal testing machine. Figure 11 shows the curve of shear strength as a function of power. From the figure, it can be observed that as laser power increases from 150 W to 250 W, shear strength increases with increasing power. However, at 300 W, shear strength sharply decreases. The reason for this is that at excessively high laser power, beyond a certain threshold, the depth of the weld pool increases continuously. This leads to more glass entering the weld pool and mixing with molten metal, increasing stress on the glass side. Moreover, a higher energy input raises the welding temperature, and combined with the poor thermal conductivity of glass, heat tends to accumulate at the glass side of the weld, further increasing stress and making the glass brittle. Additionally, the inherent reduction in material strength due to reduced glass material can decrease its tolerance to stress.

3.4. Impact of Frequency on Welding Strength of Glass and Aluminum Alloy

The frequency of a pulsed laser refers to the number of times the laser operates within a unit time, as illustrated in Figure 12. In this experiment, the unit time is one second. When the welding speed remains constant, changing the frequency effectively alters the density of the laser spots along the welding path, which affects the overlap of the laser beams. Therefore, varying the frequency can significantly influence the welding outcome.

To investigate how changes in frequency affect welding results and to determine the most suitable welding parameters, Nd: YAG was used to weld aluminum alloy and glass under the experimental conditions listed in Table 4, experiment numbers 17 to 24. The weld seam morphology under different frequencies is shown in Figure 13. From the images, it is observed that as the frequency increases, there is little change in the depth of fusion, but significant differences in the cross-sectional morphology of the weld seam. At a frequency

of 8 Hz, the cross-sectional area of the entire weld pool is smaller. As the frequency increases beyond 12 Hz, noticeable cracks appear on the glass side and significant voids can be seen at the weld seam.

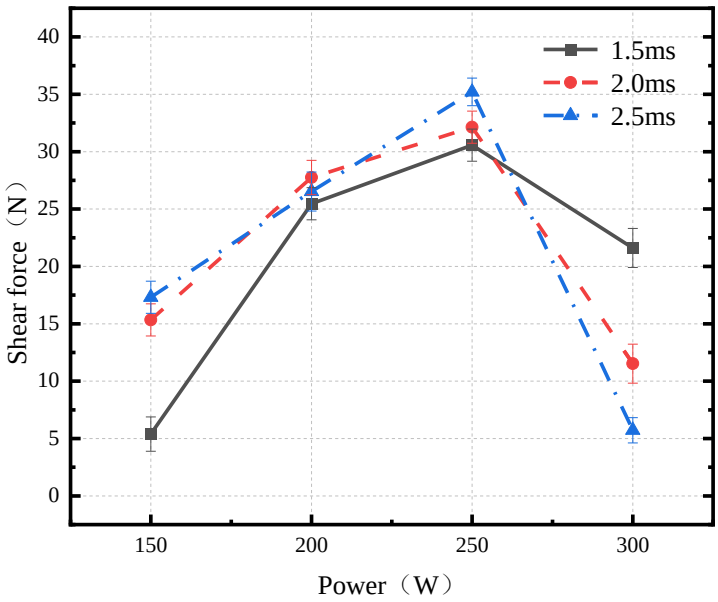

Figure 11. Shear force variation with welding power curve.

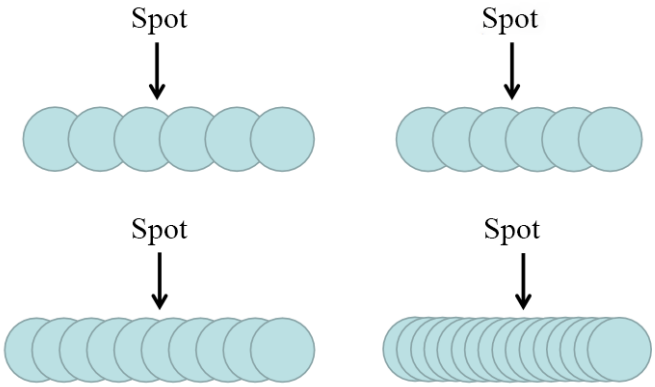

Figure 12. Schematic of beam overlap at different frequencies during welding.

The cross-sectional images of the weld seam after shear strength testing were observed under a SEM, as shown in Figure 14. It is observed from the images that with increasing frequency, there is a significant increase in aluminum alloy splattering around the weld seam. Additionally, the morphology of adhered material on the aluminum alloy side transitions from large chunks to finer fragments as the frequency increases. The reason behind this observation is that increasing frequency subjects the glass to more frequent energy impacts within the same volume. However, excessively high frequencies can lead to significant accumulation of heat, contributing to increased internal stress and crack formation within the glass.

Since frequency and power are closely related parameters that significantly impact the energy input during welding, the relationship derived from one set of power parameters may not necessarily apply to other power settings. To better analyze the influence of frequency on welding and establish a more general rule, additional welding experiments were conducted by varying the frequency at powers of 200 W and 300 W. The shear strength versus frequency curve is shown in Figure 15. The maximum shear strength of 35.21 N was achieved at a frequency of 10 Hz. The trend of shear strength change under different

power conditions is similar, with shear strength increasing initially and then decreasing as frequency changes.

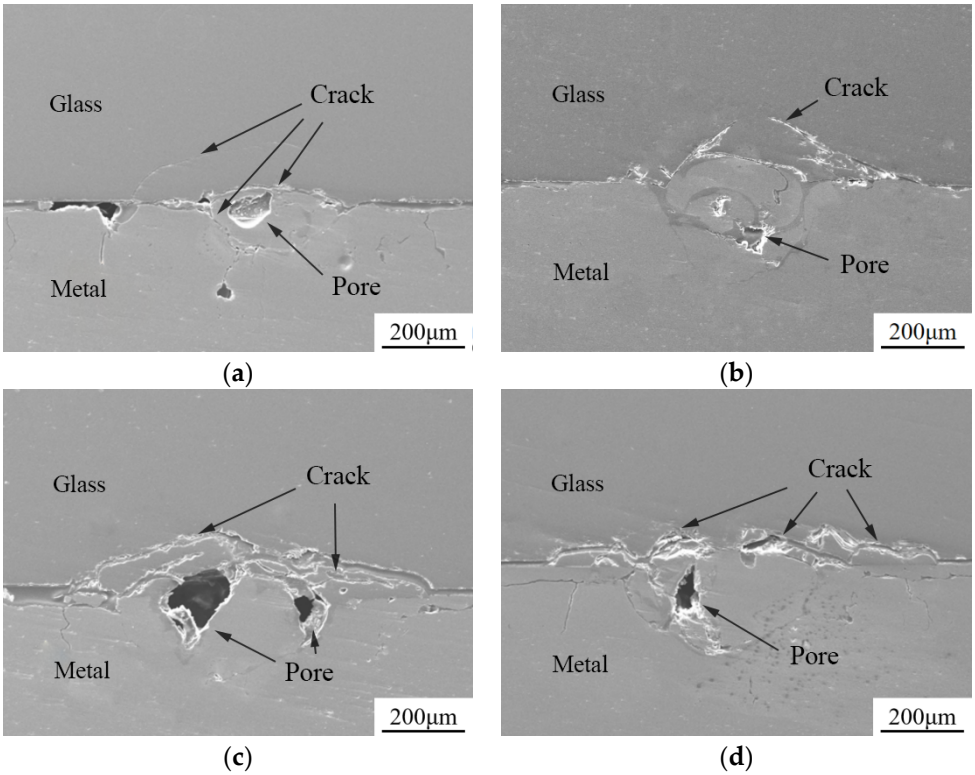

Figure 13. Weld seam cross-section images at different frequencies. (**a**) Frequency 8 Hz. (**b**) Frequency 10 Hz. (**c**) Frequency 12 Hz. (**d**) Frequency 14 Hz.

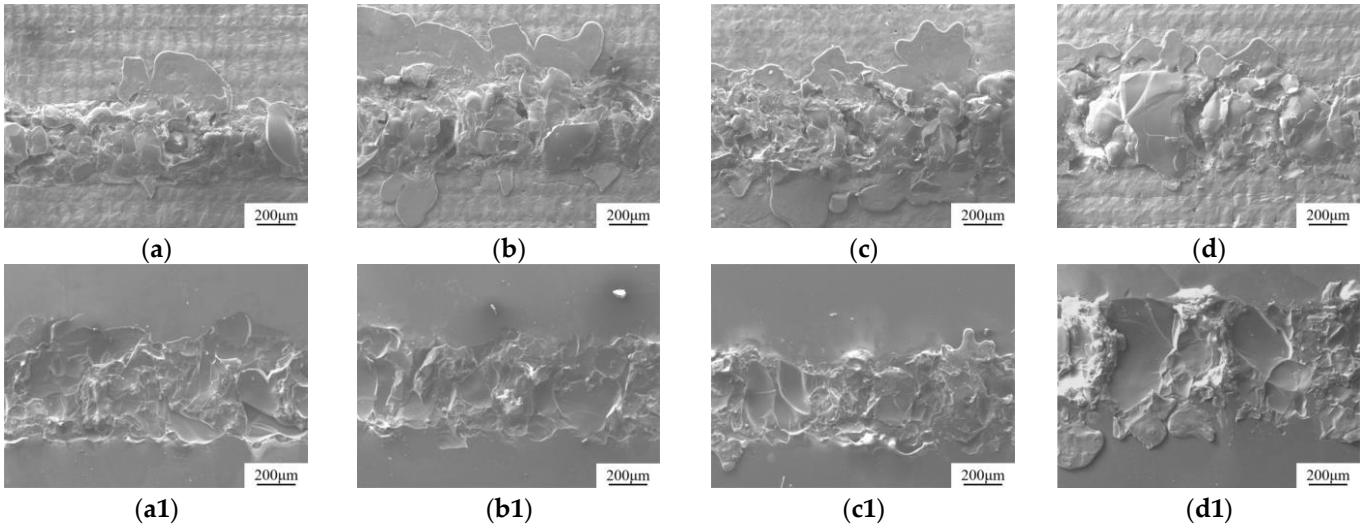

Figure 14. Weld fracture images at different frequencies. (**a**,**a1**) Frequency 8 Hz. (**b**,**b1**) Frequency 10 Hz. (**c**,**c1**) Frequency 12 Hz. (**d**,**d1**) Frequency 14 Hz. (**a**–**d**) Metal side. (**a1**–**d1**) Glass side.

According to Formula (2), we can see that at a fixed laser power, the energy density per pulse increases as the pulse frequency decreases. At a frequency of 8 Hz, the energy per pulse is too high and the interval time is long. This leads to significant thermal cycling of the glass, causing excessive stress and affecting welding quality. Meanwhile, the aluminum alloy does not retain sufficient heat, resulting in inadequate melting due to the short duration of heating. On the other hand, at a higher frequency of 14 Hz, although the energy

per pulse is reduced, the high overlap of laser spots causes repeated welding, leading to unstable welding quality and a significant drop in post-weld shear strength.

$$P_{avg} = E_p f \tag{2}$$

where P_{avg} is the average power (W). E_p is the energy per pulse (J). f is the frequency (Hz).

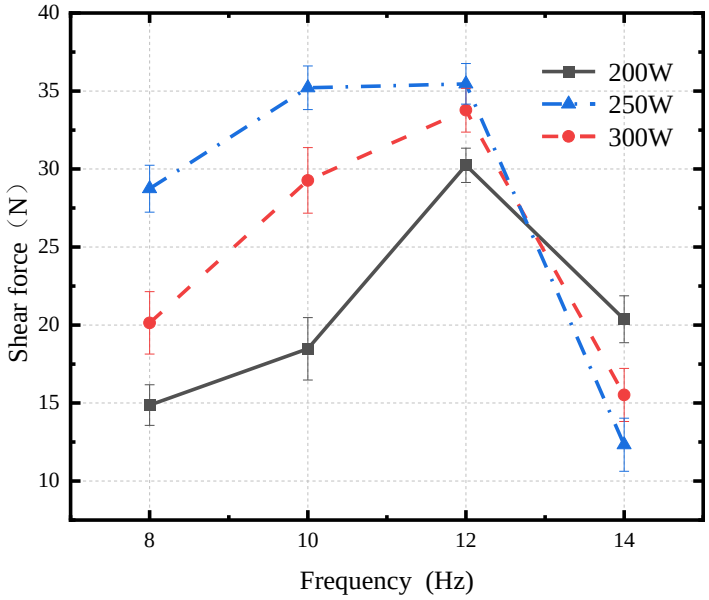

Figure 15. Shear strength variation with welding frequency.

3.5. Influence of Pulse Width on the Welding Strength of Glass and Aluminum Alloy

Pulse width, or pulse duration, refers to the length of time a pulse lasts. In laser welding, it can be understood as the duration the laser operates at maximum power. When laser power, frequency, and speed are kept constant, increasing the pulse width allows the welded material more time to absorb energy, thereby also affecting the amount of energy absorbed. To investigate the impact of pulse width on welding, experiments were conducted with pulse widths of 1.5 ms, 2.0 ms, 2.5 ms, and 3.0 ms, while keeping other laser parameters constant at 200 W power, 10 Hz frequency, 0 mm defocus, and 1 mm/s welding speed, as shown in Table 4, serial numbers 25–36.

During welding, it was found that with a pulse width of 1.5 ms, successful welding could not be achieved; the welded samples were very brittle and almost had no shear strength. Laser power primarily affects the energy output of the laser, while pulse width influences the duration of laser exposure. Keeping the same power and welding speed, increasing the pulse width extends the laser's action time on the aluminum alloy and glass. Welded samples with pulse widths of 2.0 ms, 2.5 ms, and 3.0 ms were embedded in resin, then cut, ground, and polished. The weld cross-sections were observed under a SEM, as shown in Figure 16. From the figure, it can be observed that as the frequency increases, the change in penetration depth is minimal. However, there is a significant difference in the weld seam cross-sectional morphology. When the pulse width is 1.5 ms, the cross-sectional area of the molten pool is relatively small. As the pulse width increases to more than 3.0 ms, noticeable cracks appear on the glass side, and there are prominent pores in the weld seam.

The welded samples were observed under an electron microscope to examine the fracture surface, as shown in Figure 17. From the images, it can be observed that at a pulse width of 2.0 ms, the fracture is neat and uniform, with no significant spatter around the edges. At a pulse width of 2.5 ms, the weld seam's width increases noticeably, and there is a large area of spatter around the weld, due to the increased energy. At 3.0 ms, the fracture becomes fragmented and no large spatter areas are present. This phenomenon occurs because increasing the pulse width significantly raises the energy during welding

and extends the welding time. This allows for a longer period of material flow between the molten aluminum alloy and the softened glass. However, at 3.0 ms, the prolonged energy input leads to excessive heating of the glass, which, having a lower thermal expansion coefficient, accumulates too much heat, causing the glass to crack due to thermal stress.

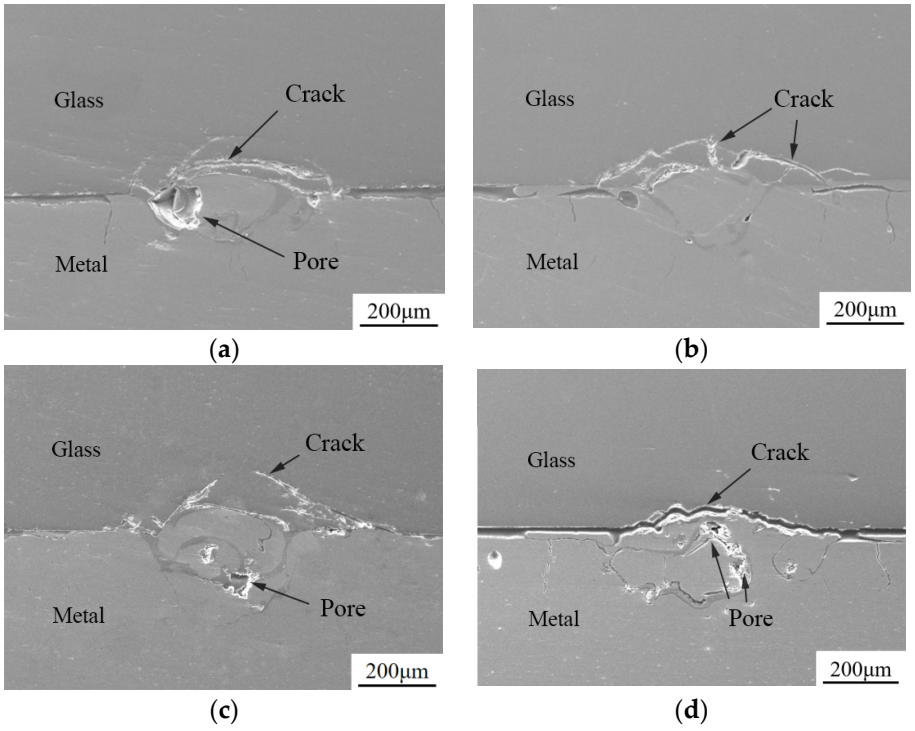

Figure 16. Images of welded fracture at different pulse widths. (**a**) Pulse width 1.5 ms. (**b**) Pulse width 2.0 ms. (**c**) Pulse width 2.5 ms. (**d**) Pulse width 3.0 ms.

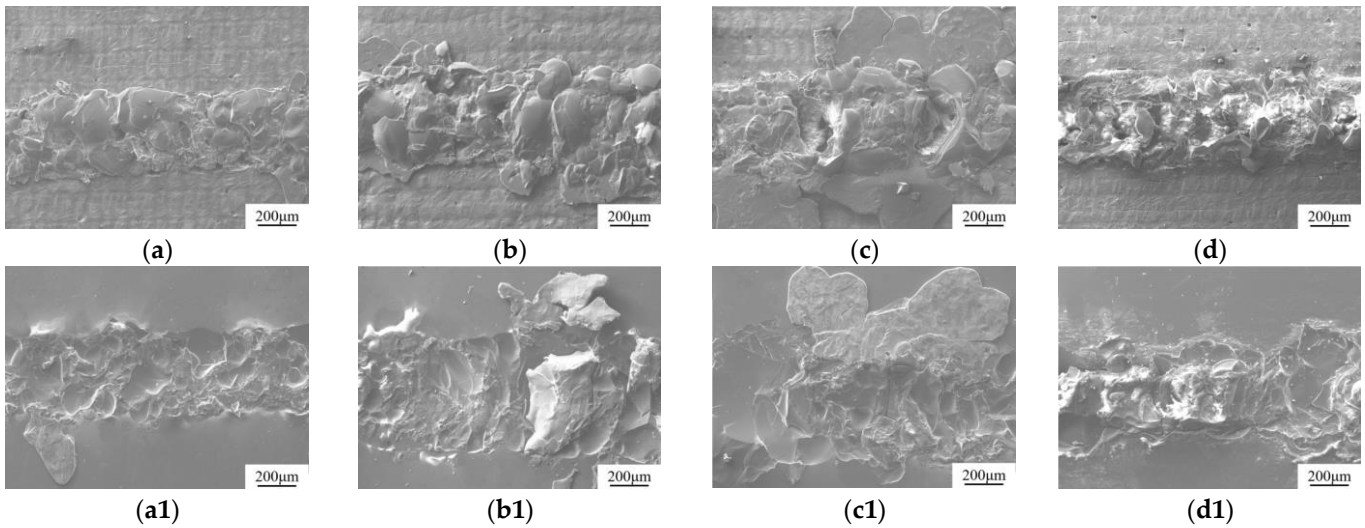

Figure 17. Images of welded fracture at different pulse widths. (**a**,**a1**) Pulse width 1.5 ms. (**b**,**b1**) Pulse width 2.0 ms. (**c**,**c1**) Pulse width 2.5 ms. (**d**,**d1**) Pulse width 3.0 ms. (**a**–**d**) Metal side. (**a1**–**d1**) Glass side.

Additional tests on shear force variation with pulse width were conducted at 200 W and 300 W. It was found that the trend of shear force variation was the same at each power level. The curve of shear force variation with pulse width is shown in Figure 18. The figure indicates that as the pulse width increases, the shear force first increases and then decreases, with the maximum shear force occurring at 2.5 ms.

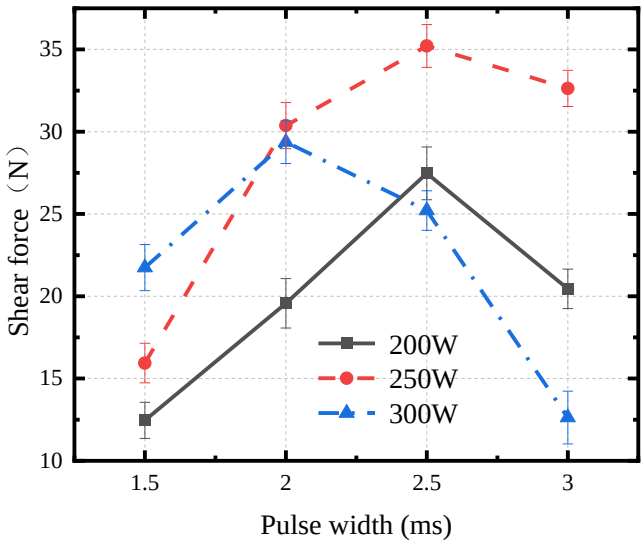

Figure 18. Curve of shear force variation with pulse width.

The reason for the variation in shear force is that as the pulse width increases, both the aluminum alloy and the glass receive more heat, resulting in longer melting and bonding times. However, due to the significant difference in thermal expansion coefficients between high borosilicate glass and aluminum alloy, once the threshold is exceeded and too much energy accumulates on the surfaces of the glass and aluminum alloy, the glass may develop internal cracks due to excessive stress. Therefore, an appropriate pulse width should be chosen in the experiment.

4. Discussion

In previous sections, the effects of different laser process parameters on the welding strength of samples and the changes in fracture morphology were discussed in detail. This section explores the causes of shear fractures in welded samples by examining the 3D morphology and elemental distribution of the weld fractures.

X-ray diffraction (XRD) is a technique used to analyze the crystal structure of materials, typically employed for studying the lattice structure of crystals, and for qualitative and quantitative crystallographic analysis. The main components of high borosilicate glass are boron oxide and silicon dioxide, both of which are amorphous. When using XRD for detection, a broad background rather than distinct diffraction peaks will be observed. Figure 19 shows the X-ray diffraction patterns of fracture surfaces on the aluminum alloy and high borosilicate glass sides. From the phase analysis results, it was found that the glass-side fracture contains a small amount of Al, which is due to aluminum alloy splashes peeling off and adhering to the glass during the shear test. The fracture on the aluminum alloy side mainly consists of the Al phase, indicating no chemical changes occurred to form new substances during welding. From the surface scan results of the fractures, it can be seen that glass residues often remain on the aluminum alloy side of the fracture. However, since the main components of glass are not suitable for XRD detection, no distinct glass components were found in the XRD results of the aluminum alloy side fractures.

The principle of the confocal color electron microscope is to use a laser light source to excite fluorescence within the sample and focus the confocal optical path at different depths of the sample. The reflected data are then integrated to generate multi-depth images. Since glass is highly transparent, using a confocal color electron microscope for 3D morphology analysis of glass results in significant distortion. Therefore, this paper primarily analyzes the 3D morphology of the fracture on the aluminum alloy side. The 3D contour analysis of the fractures after shear strength testing of samples prepared with different laser process parameters is shown in Figure 20.

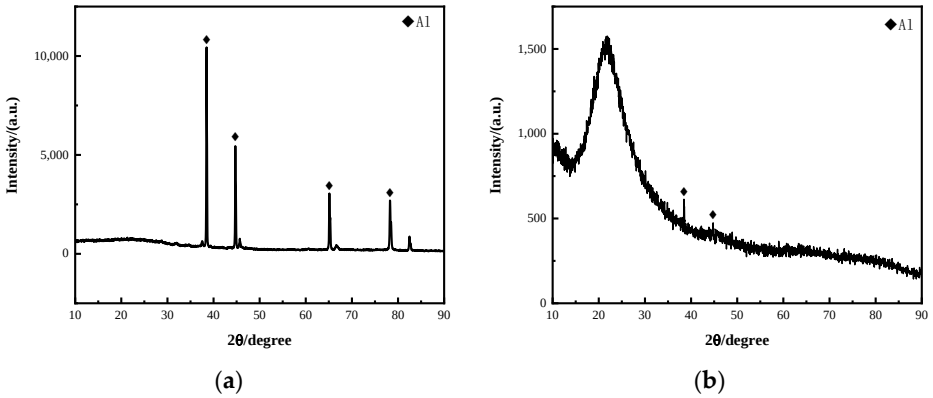

(**a**) (**b**)

Figure 19. X-ray diffraction patterns of fracture surfaces on aluminum alloy and high borosilicate glass sides. (**a**) Metal side. (**b**) Glass side.

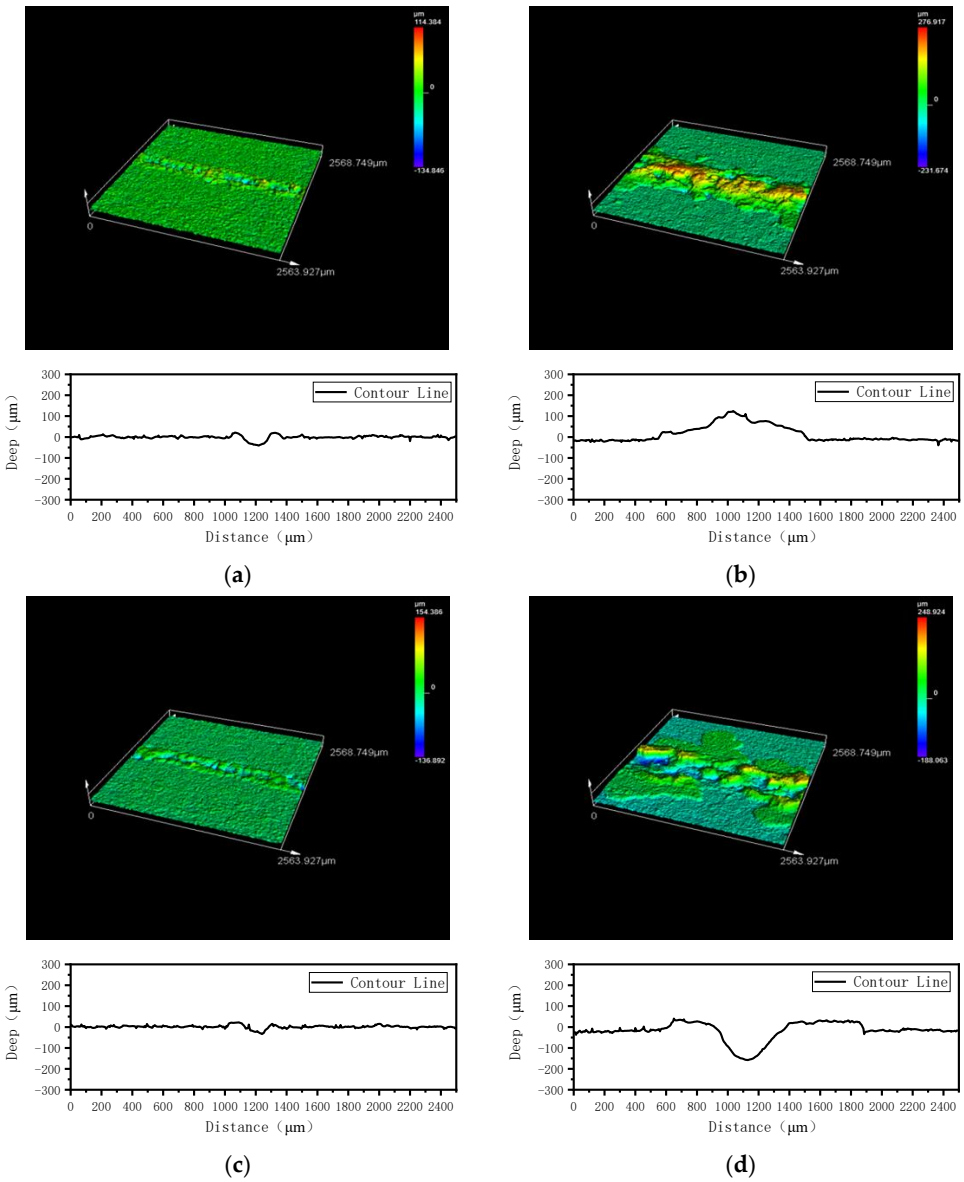

(**a**) (**b**)

(**c**) (**d**)

Figure 20. 3D morphology and contour curves of metal and glass side fractures after shear testing of welded samples with different laser process parameters. (**a**) Laser power 150 W. Frequency 10 Hz. (**b**) Laser power 300 W. Frequency 10 Hz. (**c**) Laser power 250 W. Frequency 8 Hz. (**d**) Laser power 250 W. Frequency 14 Hz.

In Figure 20a, the 3D morphology and corresponding contour curves along the dashed line of the metal side after shearing a welded sample with power 150 W, frequency 10 Hz, defocus amount 0 mm, and welding speed 1 mm/s are shown. It can be observed that the fracture area on the metal side is lower than the metal surface, with a depression depth of about 40 μm and a fracture width of approximately 250 μm. Compared to the 3D morphology of fractures under other parameters, this fracture is narrower. When the laser power is increased to 300 W, the fracture morphology, as shown in Figure 20b, differs from other parameters in that the fracture area shows many protrusions without depressions. Contour analysis reveals that the residual material is about 124 μm higher than the metal surface, and the fracture width is approximately 900 μm, significantly wider than under lower laser power. Additionally, many splashes slightly higher than the aluminum alloy surface can be observed around the fracture, identified in previous studies as aluminum alloy splashes. Figure 20c,d show the 3D morphology and corresponding contour curves along the dashed line of the metal side after shearing welded samples with power 250 W, defocus amount 0 mm, and pulse width 2.5 ms, with frequency changes. When the frequency is 8 Hz, the fracture morphology is similar to that under lower power, with the fracture area depressed below the aluminum alloy surface. However, under this parameter, the depression is larger and wider due to the higher power and greater energy at a single point. Increasing the frequency to 14 Hz, as shown in Figure 20b, changes the 3D morphology of the fracture from a single depression to a state of both depressions and protrusions. The depression depth can reach up to 157 μm, significantly deeper than under lower power, with protrusions mainly distributed on both sides of the fracture and depressions concentrated in the central region.

Figures 21 and 22 shows the EDS (Energy Dispersive X-ray Spectroscopy) surface scan results of the metal and glass side fractures. From the figure, it can be observed that the splatter consists mainly of Al elements, indicating that the metal matrix melts and splatters under laser action. The splatter not only remains on the metal side fracture but also adheres to the glass side. Conversely, the adherent material at the aluminum alloy fracture is primarily glass.

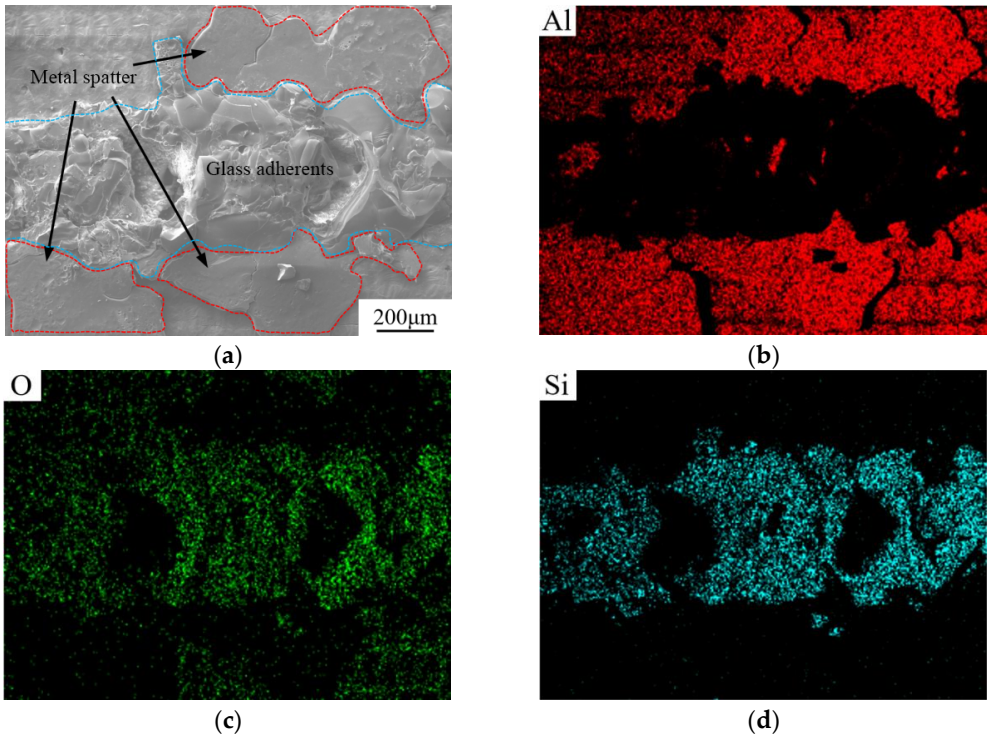

Figure 21. EDS surface scan analysis of fracture on metal side. (**a**) Surface morphology of the metal side. (**b**) EDS spectrum of element Al. (**c**) EDS spectrum of element O. (**d**) EDS spectrum of element Si.

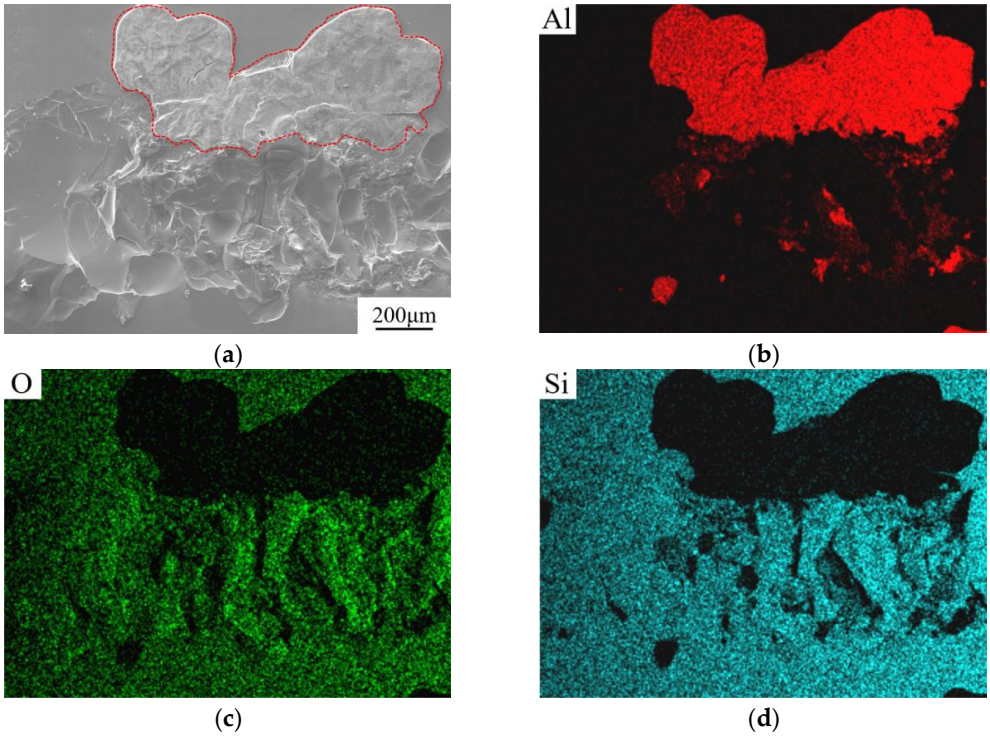

Figure 22. EDS surface scan analysis of fracture on glass side. (**a**) Surface morphology of the glass side. (**b**) EDS spectrum of element Al. (**c**) EDS spectrum of element O. (**d**) EDS spectrum of element Si.

The material distribution at the weld seam cross-section is shown in Figure 23. Results from EDS spectroscopy testing in the figure indicate that a small amount of glass component is prominently observed in the middle and bottom of the fusion zone, suggesting effective mixing of glass with the aluminum alloy in the molten pool. Additionally, minor cracks appear on the glass side above the fusion zone, caused by stress, which is also a primary reason for fracture occurring on the glass side during shear strength testing.

Combining the three-dimensional morphology of the fracture surfaces from shear strength testing and the comparison of elemental distributions, three types of fracture locations can be summarized: fracture on the metal side, fracture at the interface between metal and glass, and fracture within the glass. Due to the thermal expansion coefficient of the aluminum alloy oxide film being approximately three times that of high borosilicate glass, and with the greater disparity in thermal expansion coefficients at high temperatures, both the glass and metal oxide films experience tensile stresses due to mutual contraction during the cooling phase following the brief action of pulsed laser irradiation.

When the laser power and pulse width are low, the energy supplied by the laser to the weld seam is insufficient. The aluminum alloy melts under the influence of the laser, splashing towards both sides of the fracture, whereas the glass side, due to inadequate energy, fails to soften sufficiently to mix timely with the aluminum alloy, resulting ultimately in the formation of voids in the weld seam area. As this area is slightly closer to the metal side, the fracture surface on the metal side after shear testing exhibits concavity, as shown in Figure 24.

When the laser power and pulse width are relatively high, the increased energy results in higher temperatures on the glass side. Upon cooling, significant stress develops on the glass side, leading to the formation of cracks in the glass, as depicted in Figure 25. During shear strength testing, cracks on the glass side tend to fail first, resulting in fractures occurring on the glass side, with substantial glass adhering to the aluminum alloy side, as shown in Figure 25.

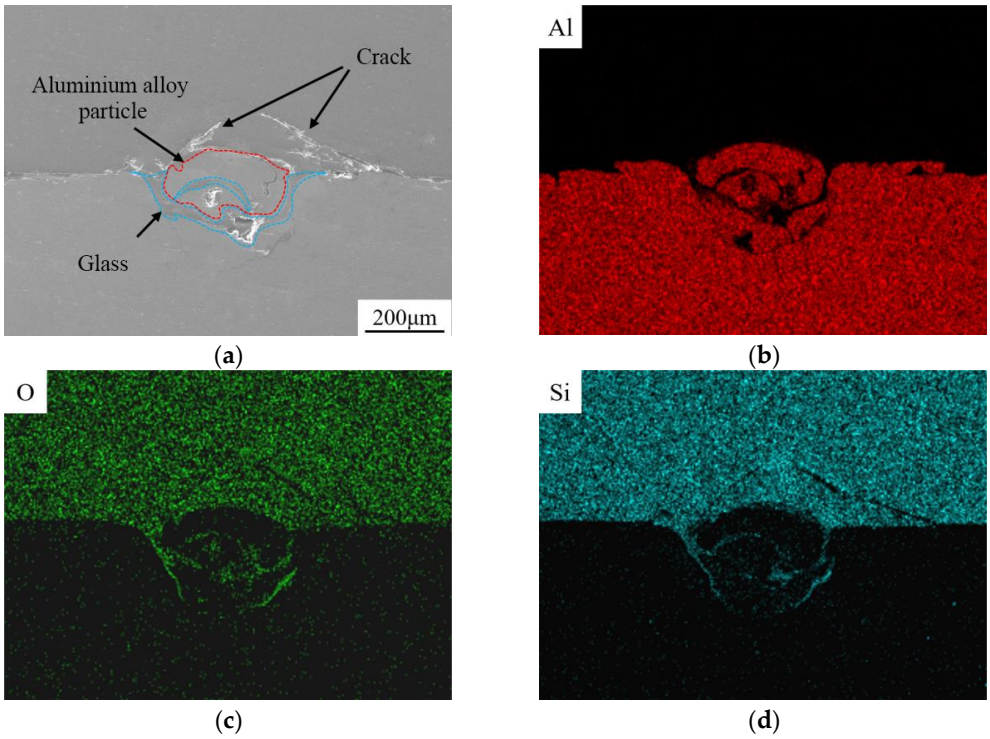

Figure 23. Material distribution at weld seam cross-section. (**a**) Surface morphology of weld seam cross-section. (**b**) EDS spectrum of element Al. (**c**) EDS spectrum of element O. (**d**) EDS spectrum of element Si.

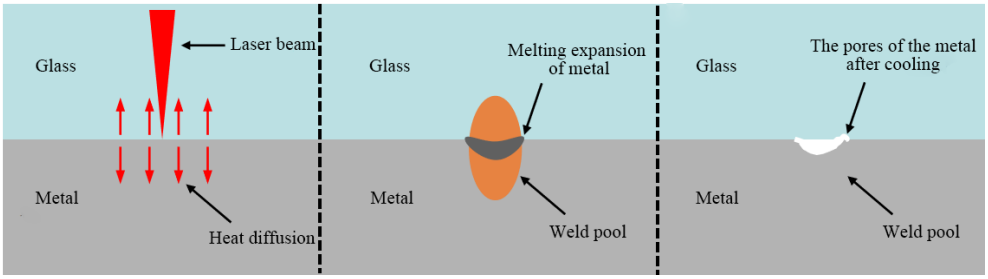

Figure 24. A schematic diagram of the welding process shows the fracture surface on the metal side.

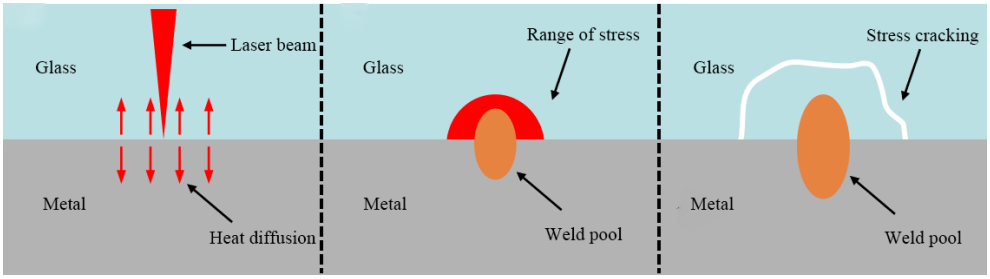

Figure 25. A schematic diagram of the welding process illustrates the fracture surface on the glass side.

When the laser power and pulse width are both reasonably adjusted, increasing the frequency appropriately can enhance the insulation time during welding, thereby reducing stress on the glass. Under these optimal welding parameters, the fracture occurs at the interface between the aluminum alloy and the glass. At this position, the shear strength test results also show higher values, indicating an ideal fracture location. However, if the frequency is excessively increased, the accumulation of energy on the glass side during welding can lead to higher stress levels.

5. Conclusions

This study utilized laser remelting surface treatment on aluminum alloy surfaces to investigate the effects of four process parameters—defocus amount, laser power, frequency, and pulse width—on the welding outcome. The main conclusions are listed in the following description:

(1) With the continuous increase in defocusing amount, the shear force test results first increase and then decrease. The welding effect is optimal when the defocusing amount is 0 mm;

(2) As the power increases, the fracture becomes noticeably wider, and the amount of spatter increases significantly. It can also be observed that with the increase in power, the adhesion on the aluminum alloy side gradually increases, while the adhesion on the glass side gradually decreases. The shear force increases with laser power initially but decreases afterward;

(3) As the frequency increases, the morphology of the adhesive on the fracture of the aluminum alloy side gradually changes from large blocks to finer fragments. The increase in frequency causes the glass to be subjected to more energy impacts within the same volume, and excessively high frequency leads to significant heat accumulation. These two factors together result in an increase in the internal stress and number of cracks within the glass;

(4) Increasing the pulse width can significantly enhance the energy during welding, and a higher pulse width allows for longer welding times, which helps to extend the duration of material flow between the molten aluminum alloy and the softened glass. However, when the pulse width is too large, the prolonged duration of energy input causes the aluminum alloy to melt more thoroughly and blend more completely with the glass. However, due to the excessive heat received by the glass and its low thermal expansion coefficient, excessive heat accumulation can cause damage and cracking of the glass.

Author Contributions: Conceptualization, C.C. and M.Z.; Data curation, C.C.; Formal analysis, C.C.; Investigation, M.Z.; Methodology, C.C. and M.Z.; Resources, M.Z.; Software, C.C.; Supervision, W.Z.; Validation, C.C. and J.T.; Visualization, J.T. and W.Z.; Writing—original draft, C.C.; Writing—review and editing, J.T. All authors have read and agreed to the published version of the manuscript.

Funding: We would like to appreciate Jiangsu Province Key Research and Development Program (Grant No. BE2021049), the Open Fund for State Key Laboratory of Advanced Welding and Joining, Harbin Institute of Technology [Grant No. AWJ-23Z01], the Open Fund for Jiangsu Key Laboratory of Advanced Manufacturing Technology [HGAMTL-2204], and the Open Fund for National Key Laboratory for Remanufactury [Grant No.xxx].

Data Availability Statement: The original contributions presented in the study are included in the article, further inquiries can be directed to the corresponding author/s.

Acknowledgments: The authors also extend their gratitude to those who provided assistance during the experimental process. The personnel are as follows: Yikai Lu from Laser Processing Research Center, School of Mechanical and Electric Engineering, Soochow University, Suzhou 215131, China. Chunlei Li from Yunnan Kunchuan Machinery Manufacturing Co., LTD., Kunming 650236, China. Chen Tian form School of Environment and Engineering, Shenyang University of Technology.

Conflicts of Interest: The authors declare no conflicts of interest.

References

1. Buček, A.; Brablec, A.; Kováčik, D.; Sťahel, P.; Černák, M. Glass bond adhesive strength improvement by DCSBD atmospheric-pressure plasma treatment. *Int. J. Adhes. Adhes.* **2017**, *78*, 1–3. [CrossRef]
2. Szesz, E.M.; Lepienski, C.M. Anodic bonding of titanium alloy with bioactive glass. *J. Non-Crystaline Solids* **2017**, *471*, 19–27. [CrossRef]
3. Tan, M.; Ling, X. Analysis of Parameters Affecting Residual Stress in Glass-to-Metal Vacuum Brazed Joints. *Trans. China Weld. Inst.* **2012**, *33*, 21–24.

4. Jia, L.; Li, Z.; Li, H.; Wolfgang, T. Effect of Intermediate Layer on Bonding Properties of Kovar Alloy 4J29/Molybdenum Glass DM308 Laser Welded Joints. *Trans. China Weld. Inst.* **2018**, *39*, 5–9.
5. Ying, H. Feasibility Analysis of the Float Process for High Borosilicate Glass Production. *China Glass.* **2008**, *29*, 12–16.
6. Pan, S. Application and Development Prospects of Borosilicate Glass. *Henan Build. Mater.* **2009**. [CrossRef]
7. Deng, X.; Wang, K.; Shi, W. Constitutive Model and Numerical Simulation of the Quenching Process of ZL205A Aluminum Alloy. *J. Heat Treat.* **2021**, *42*, 125–136.
8. Zaffaina, L.; Alain, R.; Bonollo, F.; Fan, Z. New challenges and directions for high pressure die-cast magnesium. *Metall. Ital.* **2009**, *3*, 25–29.
9. Lu, G. Analysis of laser welding technology for automotive plastic component. *Foreign Plast.* **2013**. [CrossRef]
10. Karim, M.A.; Park, Y.D. A review on welding of dissimilar metals in car body manufacturing. *J. Weld. Join.* **2020**, *38*, 8–23. [CrossRef]
11. Balestriere, M.; Schuhladen, K.; Seitz, K.H.; Boccaccini, A.; Cere, S.; Ballarre, J. Sol-gel coatings incorporating borosilicate bioactive glass enhance anti corrosive and surface performance of stainless steel implants. *J. Electroanal. Chem.* **2020**. [CrossRef]
12. Wang, H.Z. The Research on the Laser Coloring Mechanism of Stainless Steel and Its Practical Applications. Master's Thesis, Shandong University, Jinan, China, 2022.
13. Li, J.; Yang, Y.; Ren, Y.; Dong, J.; Yang, K. Effect of cold deformation on corrosion fatigue behavior of nickel-free high nitrogen austenitic stainless steel for coronary stent application. *J. Mater. Sci. Technol.* **2018**, *34*, 660–665. [CrossRef]
14. Lei, D.; Wang, Z.; Li, J. The calculation and analysis of glass-to-metal sealing stress in solar absorber tube. *Renew. Energy* **2010**, *35*, 405–411. [CrossRef]
15. Ciuca, O.P.; Carter, R.M.; Prangnell, P.B.; Hand, D.P. Characterization of weld zone reaction dissimilar glass-to-aluminum pulsed picosecond laser welds. *Materials* **2016**, *120*, 53–62.
16. Lin, H.K.; Hong, S.Z.; Chung, B.F.; Lin, R.C. Characterization of local laser bonding quartz to anodic aluminum oxide in light emission device. *J. Opt. Quantum Electron.* **2017**, *49*, 1–8. [CrossRef]
17. Qiu, Z.L. The Research on Laser Welding Performance and Mechanism of Micro-Arc Oxidized Aluminum Alloy and High-Aluminum Ultra-Thin Glass. Master's Thesis, Southwest Forestry University, Kunming, China, 2018.
18. Li, C.Y.; Zhang, M.; Chen, C.J.; Wang, X.N.; Chen, W.G. Effects and mechanisms of laser weld spacing and welding passes on the laser sealing performance of glass and aluminum alloy. *Chin. J. Lasers* **2016**, *43*, 114–121.
19. Lu, Y.J.; Zhang, Z.L.; Liu, Y.J.; Yu, C.; Zhang, X.; Liu, X.C. Improving mechanical properties and corrosion behavior of biomedical Ti-3Zr-2Sn-3Mo-25Nb alloy through laser surface remelting. *Surf. Coat. Technol.* **2024**, *490*. [CrossRef]
20. Chen, R.; Wang, H.; Li, J.; He, B.; Shao, W.; Zhang, S. Effect of laser remelting and heat treatment on microstructure and wear resistance of 2A97 Al-Li alloy. *Surf. Interfaces* **2022**, *33*. [CrossRef]
21. Lei, D.; Wang, Z.; Li, J.; Li, J.; Wang, Z. Experimental study of glass to metal seals for parabolic trough receivers. *Renew. Energy* **2012**, *48*, 85–91. [CrossRef]
22. Li, P.; Xu, X.; Tan, W.; Liu, H.; Wang, X. Improvement of Laser Transmission Welding of Glass with Titanium Alloy by Laser Surface Treatment. *Materials* **2018**, *11*. [CrossRef]
23. Kuo, C.H.; Cheng, P.Y.; Chou, C.P. Matched glass-to-Kovar seals in N2 and Ar atmospheres. *Int. J. Miner. Metall. Mater.* **2013**, *20*, 874–882. [CrossRef]
24. Min, Z.; Yufei, C.; Changjun, C.; Zhaoling, Q. A new sealing technology for ultra-thin glass to aluminum alloy by laser transmission welding method. *Int. J. Adv. Manuf. Technol.* **2021**, *115*, 2017–2035. [CrossRef]
25. Sahoo, S.K.; Bishoyi, B.; Mohanty, U.K.; Sahoo, S.K.; Sahu, J.; Bathe, R.N. Effect of laser beam welding on microstructure and mechanical properties of commercially pure titanium. *Trans. Indian Inst. Met.* **2017**, *70*, 1817–1825. [CrossRef]
26. Ahn, J.; Chen, L.; Davies, C.M.; Dear, J.P. Parametric optimisation and microstructural analysis on high power Yb-fiber laser welding of Ti–6Al–4V. *Opt. Lasers Eng.* **2016**, *86*, 156–171. [CrossRef]
27. Xu, Z.Z.; Dong, Z.Q.; Yu, Z.H.; Wang, W.K.; Zhang, J.X. Relationships between microhardness, microstructure, and grain orientation in laser-welded joints with different welding speeds for Ti6Al4V titanium alloy. *Trans. Nonferrous Met. Soc. China* **2020**, *30*, 1277–1289. [CrossRef]
28. ASTM F734-17*Standard Test Method for Shear Strength of Fusion Bonded Polycarbonate Aerospace Glazing Material*, ASTM International: West Conshohocken, PA, USA, 2017. [CrossRef]
29. Susnik, J.; Grum, J.; Sturm, R. Effect of Pulse Laser Energy Density on Tic Cladding of Aluminium Substrate. *Teh. Vjesn.-Tech. Gaz.* **2015**, *22*, 1553–1560.